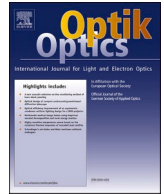




ELSEVIER

Contents lists available at ScienceDirect

Optik

journal homepage: www.elsevier.com/locate/ijleo

Original research article

Large survey camera collimation and alignment at the observation site by curvature sensing

Qichang An^a, Xiaoxia Wu^a, Xudong Lin^a, Jianli Wang^a, Tao Chen^a, Jingxu Zhang^a,
Hongwen Li^a, Liang Wang^{a,b,*}, Yansen Liu^{a,c}

^a Changchun Institute of Optics, Fine Mechanics and Physics, Chinese Academy of Sciences, Changchun 130033, China

^b School of Mechanical and Aerospace Engineering, Jilin University, Changchun 130025, China

^c Graduate University of Chinese Academy of Sciences, Beijing 100039, China

ARTICLE INFO

Keywords:

Large survey camera
Collimation
Alignment
Curvature sensor

ABSTRACT

Collimation and alignment of large survey cameras is an essential link for large survey telescope performance. A simple, stable, and fast collimation strategy is urgently needed after the correction lens assemblies are translated part-by-part at the observation site. This study proposes a method for the collimation of the correction lens assembly of a large survey telescope at the observation site. First, we investigated the method theoretically. The method was then demonstrated based on simulations in terms of reliability, while the wavefront of large transmission systems was characterized effectively. Finally, we optimized the alignment station to optimize the performance of the correction lens assembly. This study can enhance large survey telescopic developments and the design of similar large-transmission systems.

1. Introduction

To obtain detailed information about faint stars in deep space, large survey telescopes need to be constructed [1–3]. To date, dozens of survey telescopes serve as options to answer questions, such as how dark energy and dark matter influence the universe, what is the exact level of cosmic “noise,” and how asteroids “visit” Earth. One of the most powerful survey telescopes in the 2020s is the large synoptic survey telescope (LSST) [4,5]. At the same time, China’s 2.5 m survey telescope has also been under reconstruction. Through cooperation among the existing survey telescopes (VLT Survey Telescope [6], DECam [7], Visible and Infrared Survey Telescope for Astronomy [8], etc.), the universe will be mapped in more details and in wider spectrum bands.

For large survey telescopes, high imaging quality is required in the entire field-of-view (FoV) to discover the tiny geometric distortions of the galaxy introduced by “gravity lenses.” Aimed at reducing off-axis aberration, the survey camera usually contains several large lenses, and these lens assemblies are carefully aligned in the mirror lab. For example, the DECam contains five lenses, the largest of which has a diameter of 980 mm [9]. A strategy is then introduced with a rotation stage and a laser beam to align the optical corrector [10]. Furthermore, JWST investigated a method to align instruments by a set of point sources, and the range is up to one wavelength owing to the limitation of the phase retrieval algorithm [11]. However, for a larger survey instrument, its transportation can only be achieved in several parts. Considering LSST Camera as an example, its largest part has a diameter of 1.8 m. Taking China’s 2.5 m survey telescope as another example, it contains five lenses and its clear L1 aperture is 971 mm. For observations, the lenses must

* Corresponding author at: Changchun Institute of Optics, Fine Mechanics and Physics, Chinese Academy of Sciences, Changchun 130033, China.
E-mail address: wangliang.ciomp@foxmail.com (L. Wang).

<https://doi.org/10.1016/j.ijleo.2021.167273>

Received 29 November 2020; Received in revised form 31 March 2021; Accepted 20 May 2021

Available online 24 May 2021

0030-4026/© 2021 Elsevier GmbH. All rights reserved.

be collimated again one-by-one [12].

Given the size of the collimator, it is a major challenge to transfer it to the station. Moreover, at the observation site, the vibration cannot be suppressed effectively. Traditional onsite collimation always uses baseline crosstalk between optics and machine, which is unsuitable for large survey instruments. Thus, a simple and robust testing method with a large dynamic range is urgently needed to realize at-observation collimation and alignment of large survey instruments.

The direct wavefront detection method is usually based on the Shack–Hartmann wavefront sensor. However, because of the need to build a collimation and splitting optical path, the complexity of the system increases and the influences of non-common optical path aberrations become evident. Its best application scenario is on the surface of a weak scattering medium, such as an atmosphere with a small FoV, or a strong scattering medium, such as biological tissue.

At the same time, the accumulated error, which is based on the optical system design, and from the fact that the point light source is no longer located at an infinite distance, is large. Therefore, a wavefront detection method with a high-dynamic range and small vignetting effect is needed. Curvature sensing was proposed by American scientists in 1988. The technique is based on the difference in light intensity along the optical axis used to estimate the change in the wavefront curvature. Because of the direct calculation based on the light intensity transmission equation, it is not affected by uneven illumination of the pupil and by 2π phase windings. Thus, it is very suitable for optical detection of large-aperture sky survey cameras. The far-field images with the same defocus on both sides of the focal plane can be collected by a single shot. In this way, the prefocal and postfocal images can be obtained without moving parts, and simultaneous measurement can be realized. By using the characteristics of the small influence of the curvature sensing aperture, the split FoV detection can be realized, and the complete wavefront distortion information can be obtained through the synthesis algorithm.

In this article, the theoretical derivation of curvature sensing detection is conducted first. The mapping relationship between the defocused star image and lens misalignment is established and verified. Finally, using the double lens system as an example, it is collimated based on the use of the curvature of the split FoV.

2. Sensing the transmitted wavefront of large survey camera

Telescopic systems commonly use the mirror surface deformation error to evaluate the support results for large-diameter reflective primary mirrors, and small-diameter transmission elements [13]. A formula is then derived to analyze the propagation of the wavefront.

First, a single spatial frequency wavefront is used to analyze the “single shoot,” multiple defocusing locking distance detection. Subsequently, the actual wavefront with different spatial frequencies is considered based on the previous research. By taking into consideration the typical aberration components, we analyze the capacity of multiple defocusing locking distance measurements to represent different typical aberrations in the spatial frequency domain. This provides a theoretical tool for the subsequent research studies in this area.

Starting from the wavefront of the single-phase spatial-frequency component $W(\mathbf{u},0)$ and based on the premise of locking distance, the calculation process of a typical aberration of a large aperture and a large FoV photographic Sky Survey Telescope System with multiple defocusing curvature sensors is analyzed on a step-by-step basis.

$$W(\mathbf{u}, 0) = \exp \left[j \frac{2\pi A}{\lambda} \sin(2\pi \mathbf{u} \mathbf{f}) \right] \tag{1}$$

where λ is the wavelength, A is the amplitude of the single-phase spatial frequency component, \mathbf{u} is the spatial coordinate in the pupil, and \mathbf{f} is the spatial frequency domain coordinate. According to the Fresnel diffraction formula of free space propagation, the wavefront at z_i , $W(\mathbf{u}, z_i)$ is

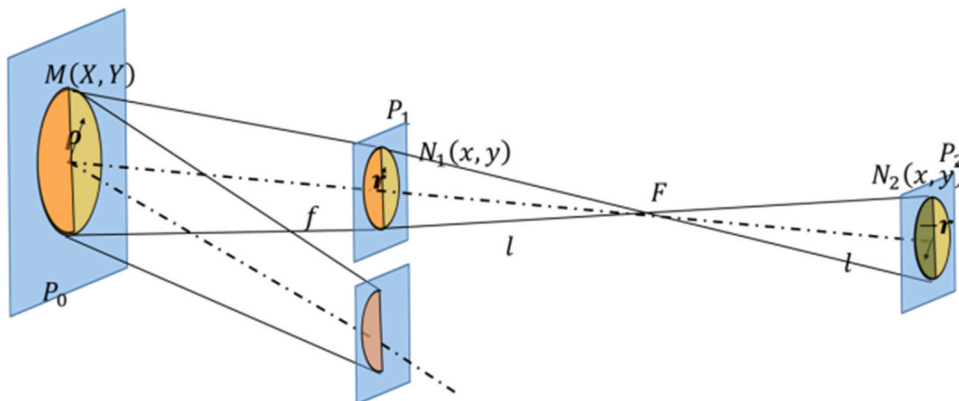


Fig. 1. Schematic of defocusing lock distance detection.

$$W(\mathbf{u}, z_i) = \exp \left[e^{j\pi|\mathbf{r}|^2 z_i} j \frac{2\pi A}{\lambda} \sin(2\pi \mathbf{u} \mathbf{f}) \right] \tag{2}$$

where z_i is the defocusing amount. The analytical expression for the detection process of multiple defocus locking distances can be established by combining Eq. (1) with Eq. (2). The relevant diagram is shown in Fig. 1.

Assuming a scalar electromagnetic field, the complex amplitude generated by the spherical wave emitted by the paraxial approximate light source can be expressed according to Eq. (3) [11],

$$\frac{\partial}{\partial z} |W(\mathbf{u}, 0)|^2 = - \left(\nabla |W(\mathbf{u}, 0)|^2 \delta_\phi(\mathbf{u}, 0) + |W(\mathbf{u}, 0)|^2 \nabla^2 W_\phi(\mathbf{u}, 0) \right) \tag{3}$$

where $|W(\mathbf{u}, 0)|^2$ is the intensity of the light field, $W_\phi(\mathbf{u}, 0)$ is the phase, ∇ is the gradient operator which denotes the slope, ∇^2 is the Laplacian operator which denotes the curvature. After discretizing the formula, the project intends to conduct theoretical research on discrete boundary curvature sensing. A disturbance is added to the wavefront, and the updated wavefront $W_\theta(\mathbf{u}, 0)$ is

$$W_\theta(\mathbf{u}, 0) = \exp[jk(A \sin(2\pi \mathbf{u} \mathbf{f} + \varphi) + \theta \sin(\omega \mathbf{u}))] \tag{4}$$

Here, θ and ω denotes the amplitude and frequency of the added disturbance, respectively. According to the Fresnel diffraction formula of free space propagation, Eq. (4) can be converted into

$$W_\theta(\mathbf{u}, z) = \exp \left[e^{j\pi|\mathbf{r}|^2 z} jk(A \sin(2\pi \mathbf{u} \mathbf{f} + \varphi) + \theta \sin(\omega \mathbf{u})) \right] \tag{5}$$

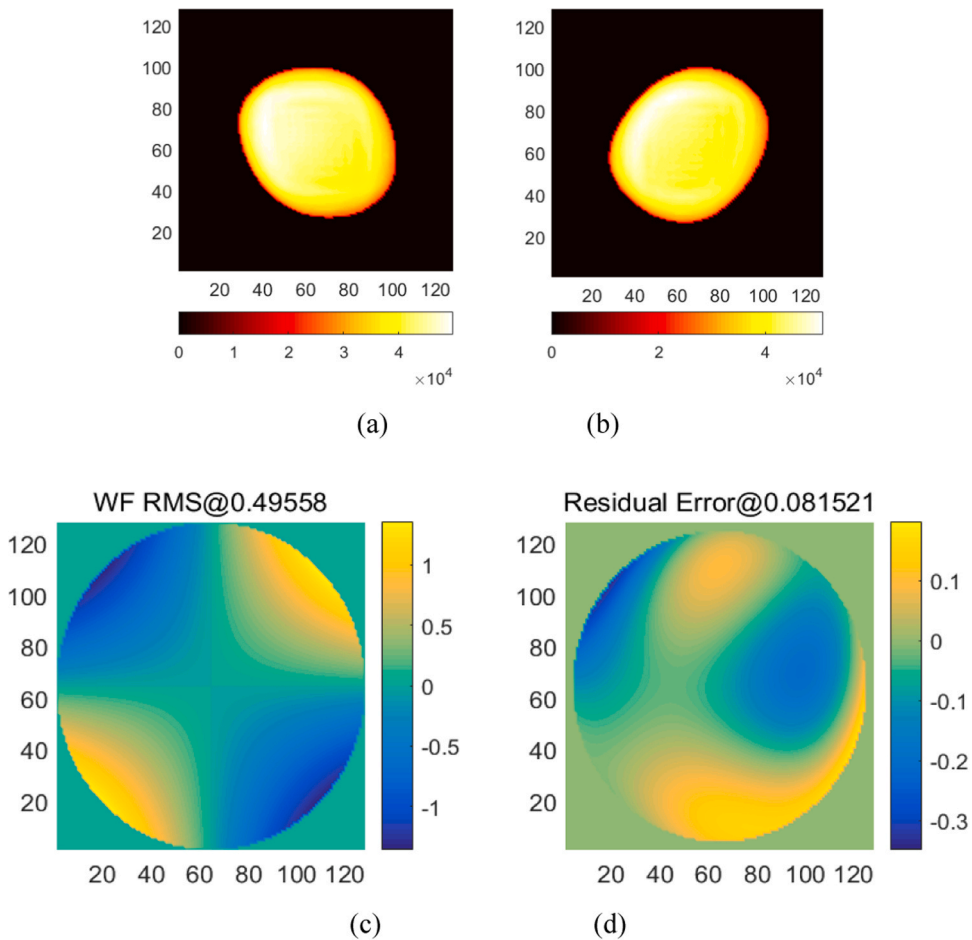


Fig. 2. Wavefront curvature sensing results.(a) Optical intensity of intrafocus position,(b) optical intensity of extrafocus position,(c) reconstructed wavefront, and(d) residual error.

$$\begin{aligned}
 W_{\theta+} &= |W_{\theta}(\mathbf{u}, z_+)|^2 \\
 &= \exp \left[e^{j\pi|\mathbf{f}|^2 z_+ \lambda} jk(A \sin(2\pi\mathbf{u}\mathbf{f} + \varphi) + \Theta \sin(\omega\mathbf{u})) \right] \\
 &\exp \left[-e^{-j\pi|\mathbf{f}|^2 z_+ \lambda} jk(A \sin(2\pi\mathbf{u}\mathbf{f} + \varphi) + \Theta \sin(\omega\mathbf{u})) \right] \\
 &= \exp \left[\left(e^{j\pi|\mathbf{f}|^2 z_+ \lambda} - e^{-j\pi|\mathbf{f}|^2 z_+ \lambda} \right) jk(A \sin(2\pi\mathbf{u}\mathbf{f} + \varphi) + \Theta \sin(\omega\mathbf{u})) \right] \\
 &= \exp \left[-2 \sin \left(\pi|\mathbf{f}|^2 z_+ \lambda \right) jk(A \sin(2\pi\mathbf{u}\mathbf{f} + \varphi) + \Theta \sin(\omega\mathbf{u})) \right]
 \end{aligned} \tag{6}$$

$$\begin{aligned}
 W_{\theta-} &= |W_{\theta}(\mathbf{u}, z_-)|^2 \\
 &= \exp \left[-2 \sin \left(\pi|\mathbf{f}|^2 z_- \lambda \right) jk(A \sin(2\pi\mathbf{u}\mathbf{f} + \varphi) + \Theta \sin(\omega\mathbf{u})) \right]
 \end{aligned} \tag{7}$$

Here, subscript + and -denotes intrafocal and extrafocal, respectively. Then, the curvature C_{θ} will be as follows.

$$\begin{aligned}
 C_{\theta} &= \frac{W_{\theta+} - W_{\theta-}}{W_{\theta+} + W_{\theta-}} \\
 &= \frac{-2Ak\pi|\mathbf{f}|^2(z)\lambda \sin(2\pi\mathbf{u}\mathbf{f} + \varphi) - k\pi|\mathbf{f}|^2(z)\lambda(\Theta_+ \sin(\omega_+\mathbf{u}) - \Theta_- \sin(\omega_-\mathbf{u}))}{1 - \lambda\pi k|\mathbf{f}|^2(\Theta_+ \sin(\omega_+\mathbf{u}) + \Theta_- \sin(\omega_-\mathbf{u}))}
 \end{aligned} \tag{8}$$

According to the process above, the Poisson equation of the Zernike mode with nonzero curvature can be simulated, and the Poisson equation based on an iterative Fourier transform is realized.

3. Simulation analysis

The wavefront sensing is conducted by using split field wavefront sensing. A hybrid strategy of physical and computational optics is used. The initial value is obtained by the traditional curvature-sensing method. The defocused star image in the FoV is iterated. The wavefront aberration is calculated by taking the morphological index of the defocused star image as feedback.

There are errors in the intrafocal and extrafocal images. In this study, the influence of different deviations on the calculation accuracy and closed-loop effect is analyzed.

As shown in Fig. 2, the coma is considered as an example. Accordingly, the calculation accuracy of the coma in the single-coma mode and compound-aberration mode is analyzed. In the first mock exam, the accuracy was higher than 2% after 20 iterations.

Herein, we use wavefront information obtained in two closed FoVs to estimate the aberration in the averaging FoV, as shown in Fig. 3(a). The closed-loop performance is investigated at different levels of aberrations, as shown in Fig. 3(b). We can see from Fig. 3(b), both the step and number of iterations decide the convergence character; however, the final accuracy is not influenced by these two factors.

The 30 m telescope (TMT) team has proposed normalized point source sensitivity analysis (PSSn) that evaluated the overall performance and surface shape of the telescope and estimated the distribution of systematic errors. It accurately shows the performance of the telescope regarding the observation time [12]. Using the optical transfer function, we can establish an estimate of the system PSSn subject to the premise of its discrete aperture collimator detection [13–15].

Expressing PSSn as a function of the optical transfer function (OTF) yields,

$$PSSn = \frac{\int |OTF_e(\vec{\theta})|^2 |OTF_{t+a}(\vec{\theta})|^2}{\int |OTF_{t+a}(\vec{\theta})|^2} \tag{9}$$

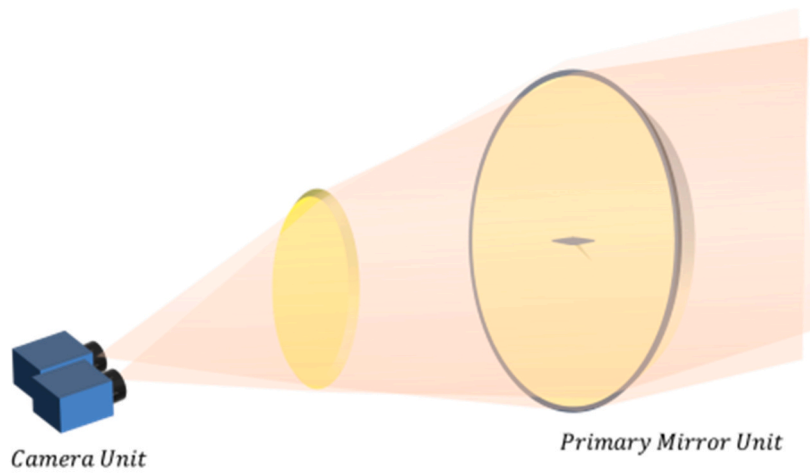
where OTF_e is the optical transfer function of the error telescope, and OTF_{t+a} denotes the optical transfer function of the ideal telescope exposed to the atmosphere.

4. Results and discussion

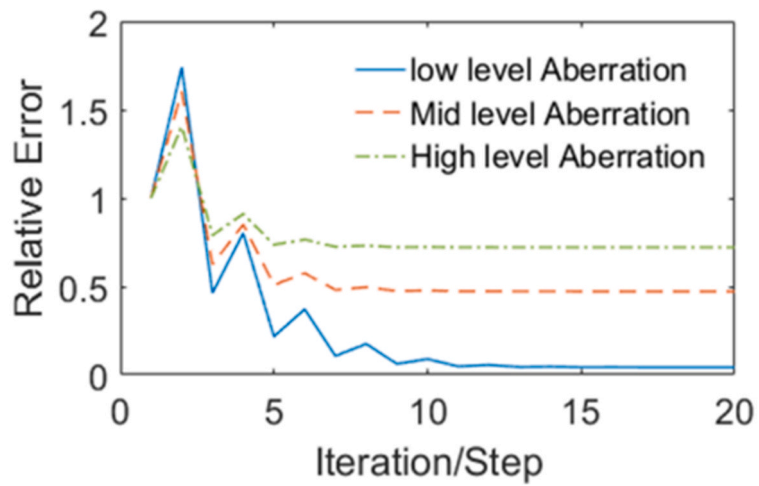
The total number and distribution of support points are the two main concerns of the support design of large-aperture lenses. Therefore, the selection of the support method and structural design is performed. Thereafter, we analyzed and calculated these two design variables, and determined the number and locations of the support points by comparing the variations in the surface root-mean-square (RMS) curve and PSSn. Initially, we optimized the number of support points of the largest aperture L1 in the correction lens group.

The wavefront was tested in two FoV, extra- and intro- focus accordingly, at a single shoot. To verify the reliability, we experimentally verified the results by the Shack–Hartmann wavefront sensor (SHWFS) as a cross-check method, which is shown in Fig. 4. In this optical layout, a deformable mirror (DM) is adopted to simulate different types of aberrations, and this DM also works as an entrance pupil with a diameter of 80 mm.

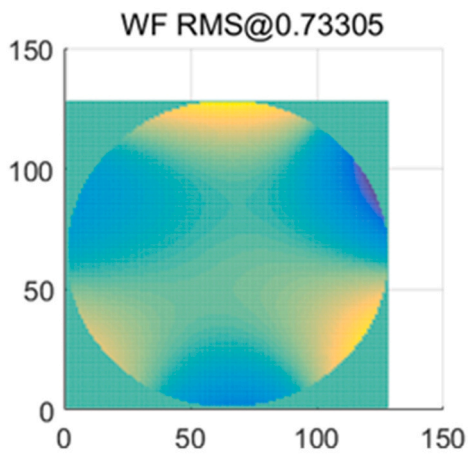
Herein, a large aperture and large FoV simulation system was constructed with the split-field wavefront for the two-lens system. The two lenses simulate the aligned system and the part to be aligned in the correcting mirror set. Accordingly, the corresponding element misalignment can be calculated based on the contrast solution. As shown in Fig. 4(b), the corresponding relationship between the one-dimensional tilt of the correcting mirror set and the result of the split-field wavefront sensing is established to verify the



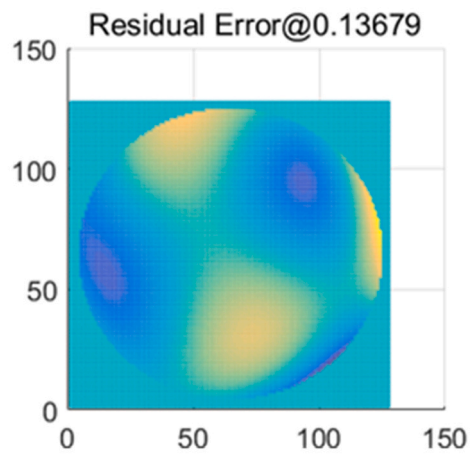
(a)



(b)



(c)



(d)

Fig. 3. Closed-loop performance of split-field wavefront curvature sensing. (a) Schematic of split-field wavefront curvature sensing, (b) residual error curves of closed-loop iteration for different level aberrations, (c) reconstructed wavefront, and (d) residual errors.

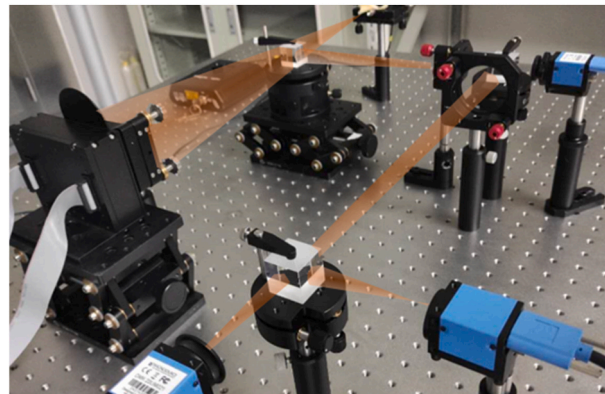
feasibility of the use of split-field wavefront sensing for the calibration of large-aperture patrol cameras subject to the condition of single-degree-of-freedom motion.

As shown in Fig. 5, lens 2 begins to move in the opposite direction after tilting two units. The defocus dot image of the adjacent FoV is then recorded in the corresponding two tilt units, one tilt unit, and the alignment state. The wavefront component is decomposed, as shown in the figure.

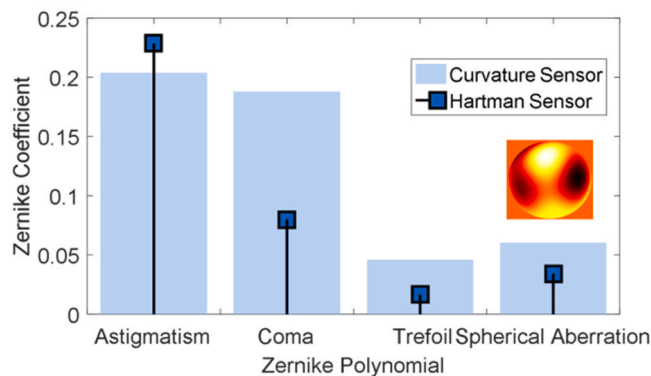
It can be observed that the coma is sensitive to the tilting of the wavefront components, and can be used as a marking aberration for tilt adjustment of single elements. For more elements, optical units can be adjusted one-by-one. Alternatively, additional marking aberrations can be measured by means of computer-aided adjustments based on sensitivity matrix [16].

For example, the Korean Research Institute of Standards and Science (KRISS) system is an integrated testing device developed by the Korean Institute of Standards and Science (KRISS), with a primary mirror diameter of 0.9 m and a focal length of 9.9 m that can test the imaging effect of systems below the meter level. The KRISS optical system takes the form of Cassegrain, and the relative relationship between primary and secondary mirrors can be calibrated manually such that the mean square root of the wavefront of the system is better than $\lambda/5$ ($\lambda = 633$ nm).

To verify the system’s reliability, we experimentally verified the correlations of PSSn at different defocusing amounts. The experimental device consists of a laser, a pupil mask, two experimental lenses, and a charge-coupled device (CCD) camera. The laser placed at some distance is used to simulate the starlight plane wave that is reflected by the main mirror followed by its transmission through the lens. The diameter of the experimental lens was 80 mm. A pupil mask was placed at the entrance pupil of the lens to indicate that the clear aperture of the lens is reduced by one-third owing to the influence of the main mirror. The experimental optical path is shown in Fig. 5. Based on the setup in Fig. 5, we conduct an experiment to verify the control effectiveness.



(a)



(b)

Fig. 4. Verification experiment of wavefront curvature sensing in split field. (a) Schematic of the verification experiment, (b) comparison of different aberrations between curvature sensor and the Shack–Hartmann wavefront sensor (SHWFS).

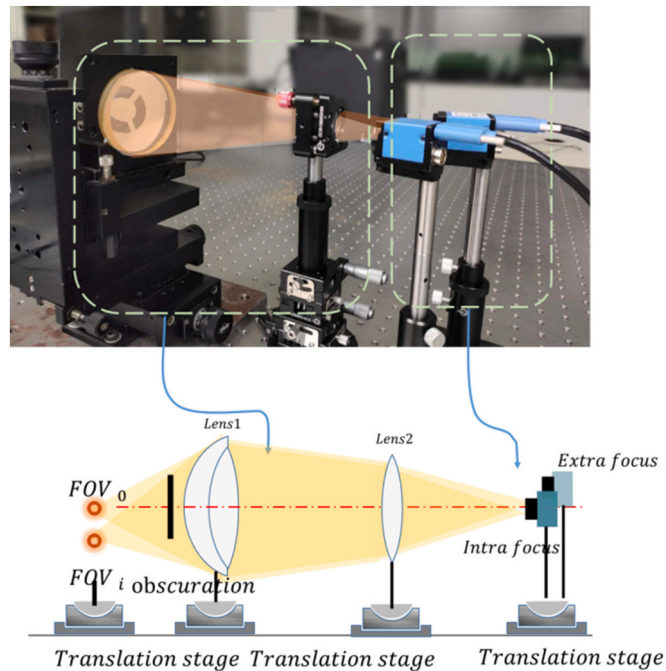


Fig. 5. Active optics experiment system based on curvature sensor.

Fig. 6 depicts the experimental process of active control of the optical aberrations. As shown in Fig. 6(a), the main low-order aberrations are controlled after three iterations.

The imaging quality decreases considerably when the extent of system misalignment increases. The change curve of the defocus extent and PSSn is shown in Fig. 6(b). The PSSn value decreases owing to the defocus. However, the trend is the same as that in the in-focus imaging case. From the experimental results, the actual situation is consistent with the variation of the full-frequency-domain variable-metric imaging quality evaluation method that exhibits reliability.

5. Conclusions

Astronomical research on black holes, dark energy, and dark matter has led to the development of large survey telescopes [17]. To achieve the scientific objectives of astronomy and space observation and ensure the final imaging effect of large telescopes, it is necessary to accurately detect and evaluate the wavefront of the integrated correction mirror group system. However, with the increase in the optical system aperture, the cost and technical risk associated with the construction of a single aperture, integrated detection device, are also increasing rapidly, and cannot meet the needs of the observatory.

This study introduced a method for correct the wavefront error and improve the imaging quality of large lens assemblies. For traditional methods, integrated detection mainly used large planar or natural stars. However, the light path can only be formed when the system is not aligned accurately, that greatly restricts its efficiency and costs.

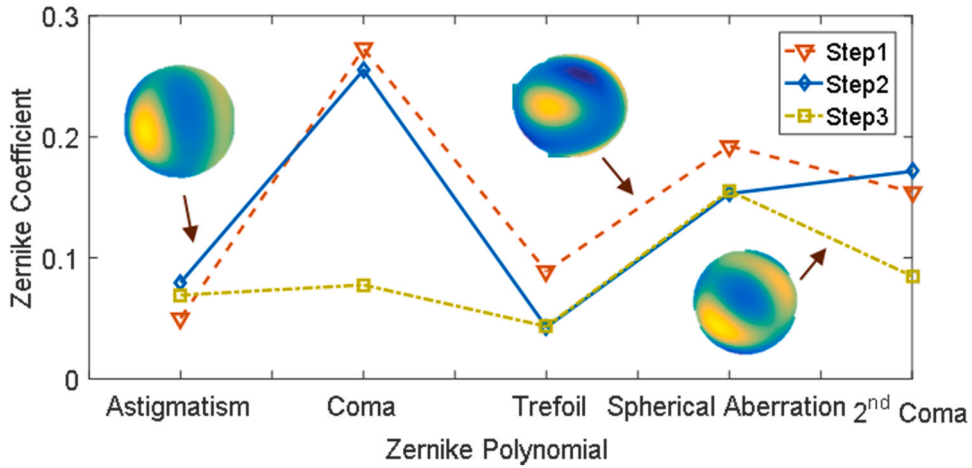
Moreover, the traditional alignment is mainly aimed at the Cassegrain system, and its theoretical modeling and numerical simulation are relatively mature. However, for a large aperture sky survey camera composed of multiple lenses, the nonlinear degree of the system is much higher than that of the existing Cassegrain telescope. Based on the characteristics of wavefront curvature sensing, which is stable, reliable, and free from interferences, the corresponding relationship between the actuator's driving distance and aberration was established based on a single degree-of-freedom drive and multi-field wavefront sensing. The extent to which the actuator ought to be adjusted can be inversely solved based on different field aberrations.

Role of the funding source

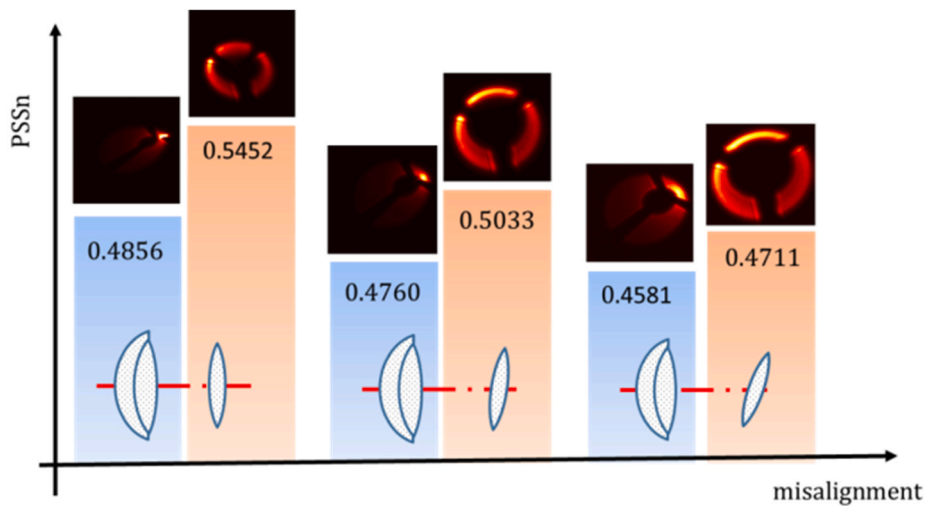
This work was supported in part by the Youth Innovation Promotion Association CAS (No. 2020221), in part by the National Natural Science Foundation of China under Grant No. 62005279, and in part by the Equipment Development Project of Chinese Academy of Sciences (YJKYYQ20200057).

CRedit authorship contribution statement

Qichang An, Xiaoxia Wu: Conceptualization. Xudong Lin: Methodology. Hongwen Li, Liang Wang: Software. Yansen Liu:



(a)



(b)

Fig. 6. Experimental results of the active optical aberration correction. (a) Active optical aberration control process.(b) PSSn at different misalignment states.

Validation. **Qichang An:** Formal analysis, Data analysis, Investigation. **Jianli Wang, Tao Chen:** Resources. **Qichang An, Liang Wang:** Writing - original draft preparation, Writing - review & editing. **Jingxu Zhang:** Supervision.

Declaration of Competing Interest

We declared that they have no conflicts of interest to this work. We declare that we do not have any commercial or associative interest that represents a conflict of interest in connection with the manuscript entitled “Large Survey Camera Collimation and Alignment at observation site by Curvature Sensing”.

Acknowledgments

This research was conducted at the Changchun Institute of Optics, Fine Mechanics and Physics, Chinese Academy of Science. The authors are very grateful to Dr. Wang for providing valuable suggestions and help. The authors also thank the two anonymous reviewers for their valuable comments.

References

- [1] Q. Guo, H. Hu, Z. Zheng, S. Liao, W. Du, S. Mao, L. Jiang, J. Wang, Y. Peng, L. Gao, J. Wang, H. Wu, Further evidence for a population of dark-matter-deficient dwarf galaxies, *Nat. Astron.* 4 (3) (2020) 1–6.
- [2] B.T. Gansicke, M.R. Schreiber, O. Toloza, N.P. Fusillo, D. Koester, C.J. Manser, Accretion of a giant planet onto a white dwarf star, *Nature* 576 (7785) (2019) 61–64.
- [3] S.-R. Núria, A. Vazdekis, F.L. Barbera, M.A. Beasley, I. Ferreras, A. Negri, C.D. Vecchia, Sub one per cent mass fractions of young stars in red massive galaxies, *Nat. Astron.* 4 (3) (2019) 1–8.
- [4] P.A. Abell, J.R. Allison, S. Anderson, J. Andrew, J.R. Angle, L. Armus, S.L. Hawley, LSST Science Book, Version 2.0, Instrumentation and Methods for Astrophysics, 2009.
- [5] G.Z. Angeli, P. Dierickx, D. Neill, et al., Overview of the LSST active optics system, *Proceedings of the SPIE* 9150, 2014; 91500 G.
- [6] R. Holzlöhner, S. Taubenberger, A.P. Rakich, et al., Focal-plane wavefront sensing for active optics in the VST based on an analytical optical aberration model, *Proc. SPIE* 9906 (2016) 99066E.
- [7] A. Roodman, K. Reil, C.J. Davis, et al., Wavefront sensing and the active optics system of the dark energy camera, *Proc. SPIE* 9145 (2014) 51–79.
- [8] R.L. Edeson, B.M. Shaughnessy, M.S. Whalley, et al., The mechanical and thermal design and analysis of the VISTA infrared camera, *Proc. SPIE* 5497 (2004) 508–519.
- [9] M. Antonik, P. Doel, D. Brooks, et al., The design and alignment of the DECam lenses and modelling of the static shear pattern and its impact on weak lensing measurements, *Optical System Alignment, Tolerancing & Verification III*. International Society for Optics and Photonics, 2009.
- [10] P. Doel, T. Abbott, M. Antonik, R. Bernstein, Design and status of the optical corrector for the DES survey instrument, *Proc. of the SPIE*, 7014, Ground-based and Airborne Instrumentation for Astronomy II, 2008; 70141 V.
- [11] Z. Koby, Z. Smith, D. Scott Acton, B.B. Gallagher, J. Scott Knight, B.H. Dean, A.S. Jurling, T.P. Zielinski, Calibration results using highly aberrated images for aligning the JWST instruments to the telescope, *Proc. of the SPIE Space Telescopes and Instrumentation Optical, Infrared, and Millimeter Wave* 9904, 2016; 990442.
- [12] Z. Lou, M. Liang, D. Yao, et al., Advanced optical design and manufacturing technology and astronomical telescopes and instrumentation - Optical design study of the wide field survey telescope (WFST), *Proc. SPIE* 10154 (2016), 101542 (A).
- [13] B. Xin, C. Claver, M. Liang, et al., Curvature wavefront sensing for the large synoptic survey telescope, *Appl. Opt.* 54 (30) (2015) 9045–9054.
- [14] Q. An, J. Zhang, F. Yang, H. Zhao, H. Cao, Normalized point source sensitivity analysis of large sparse telescopes, *Chin. Opt.* 12 (3) (2019) 567–574.
- [15] B.J. Seo, C. Nissly, G.Z. Angeli, B. Ellerbroek, J.E. Nelson, N. Sigrist, M. Troy, Analysis of normalized point source sensitivity as a performance metric for the thirty meter telescope, *Proc. SPIE* 7017 (2008) 70170 T.
- [16] E. Oteo, J. Arasa, New strategy for misalignment calculation in optical systems using artificial neural networks, *Opt. Eng.* 52 (7) (2013), 074105.
- [17] D.F. Woods, R.Y. Shah, J.A. Johnson, et al., Space surveillance telescope: focus and alignment of a three mirror telescope, *Opt. Eng.* 52 (5) (2013), 053604.